



Surface wave tomography for the Pacific Ocean incorporating seafloor seismic observations and plate thermal evolution

Takehi Isse^{a,*}, Hitoshi Kawakatsu^a, Kazunori Yoshizawa^b, Akiko Takeo^a, Hajime Shiobara^a, Hiroko Sugioka^c, Aki Ito^d, Daisuke Suetsugu^d, Dominique Reymond^e

^a Earthquake Research Institute, The University of Tokyo, Tokyo, Japan

^b Department of Earth and Planetary Sciences, Faculty of Science, Hokkaido University, Sapporo, Japan

^c Department of Planetology, Graduate School of Science, Kobe University, Kobe, Japan

^d Japan Agency for Marine–Earth Science and Technology, Yokosuka, Japan

^e Laboratoire de Géophysique CEA/DASE/LDG, Papeete, Tahiti, French Polynesia

ARTICLE INFO

Article history:

Received 28 May 2018

Received in revised form 25 December 2018

Accepted 26 December 2018

Available online xxx

Editor: M. Ishii

Keywords:

surface wave tomography

Pacific Ocean

seafloor-age dependence

oceanic upper mantle

ABSTRACT

Using broadband seismic waveforms recorded on the seafloor by more than 200 broadband ocean bottom seismometers, as well as those on land, we measured the phase speed dispersions of Love and Rayleigh waves up to the 4th higher mode to determine the three-dimensional radially anisotropic shear-wave speed structure in the upper mantle beneath the Pacific Ocean. The fastest anomalies at depths shallower than 100 km were located beneath southeast of the Shatsky Rise and strong radial anisotropy was located in the central Pacific at depths of 100–200 km. The isotropic shear-wave speed structures showed age dependence. From the age-bin-averaged shear-wave speed profiles and a half-space cooling model, we estimated the thermo-speed relationship for the Pacific Plate to construct a reference age-dependent shear-wave speed model, which was further used as an initial model for tomography iteration. Deviation maps in the Pacific Ocean from the reference model indicated that large negative residuals, which may be due to partial melting, anelasticity, and/or added heat from mantle plumes, were located along the ridges and beneath hotspots, and that large positive residuals were found beneath the northwestern Pacific Ocean. The use of an age-dependent reference model, as well as the incorporation of OBS data, greatly improves the accuracy of local phase speed estimates in tomography, as evident from a direct comparison with *in situ* array measurements.

© 2019 Elsevier B.V. All rights reserved.

1. Introduction

Plate tectonics, which is based on a relatively simple concept that a rigid lithosphere (plate) moves over a weaker asthenosphere, forms the basis of our understanding of the environment and evolution of the Earth. However, the structures and mechanisms that facilitate plate movement remain in dispute, and the elucidation of the lithosphere–asthenosphere system (LAS) has been the focus of recent geophysical studies (e.g., Kawakatsu and Utada, 2017). This is particularly true for oceanic areas, as the relatively simple nature of the creation and evolution of plates in such regions makes investigating the LAS easier than in continental areas. In seismology, a fast wave speed lid and underlying low velocity zone (LVZ) are generally associated with the lithosphere and asthenosphere, respectively, as indicated by analyses of surface waves that traverse

the ocean basins for long distances (e.g., Nishimura and Forsyth, 1989).

The Pacific Ocean has been a popular target for investigating the structure of the oceanic LAS, in regions with seafloor ages from 0 to 180 Ma. Nishimura and Forsyth (1989) showed that the shear-wave speed above a depth of 200 km progressively increases with seafloor age and follows a speed–age relationship that is qualitatively consistent with thermal cooling models of the Pacific Plate. Since then, the three-dimensional structure and age dependence of the Pacific LAS have been analyzed using regional or global surface wave tomography (e.g., Montagner and Tanimoto, 1991; Maggi et al., 2006; Nettles and Dziewonski, 2008).

In addition to the age dependence of shear-wave speeds, the age dependence of the vertical gradient of shear-wave speeds and anisotropy has been investigated. Debayle and Ricard (2013) presented a tomographic model of azimuthal anisotropy in the upper mantle, using fundamental and higher-mode Rayleigh waves, indicating that the lithosphere depth and asthenosphere transition based on azimuthal anisotropy depends on the square root of the

* Corresponding author.

E-mail address: tisse@eri.u-tokyo.ac.jp (T. Isse).

seafloor age. Burgos et al. (2014) proposed a global tomographic model of the shear-wave speed in the upper mantle including radial and azimuthal anisotropy, and investigated the lithosphere–asthenosphere boundary (LAB) beneath oceanic regions, using various vertical derivatives of their models as proxies. They observed that the depths of the proxies varied with parameter choice (i.e., isotropic speed, radial or azimuthal anisotropy) and made further inferences. Beghein et al. (2014) compared an anisotropic shear-wave tomography model with detection of the Gutenberg discontinuity to evaluate the context and relation to the LAB, and concluded that these two boundaries were not equivalent interfaces. Schaeffer et al. (2016) obtained an azimuthally anisotropic global shear-wave speed model, from the crust to the transition zone, using the fundamental and higher modes of Rayleigh waves. Using vertical variations in azimuthal anisotropy orientations as a proxy for the LAB, they reported an average LAB depth of ~ 115 km beneath the global ocean, with a clear age dependence that matched the predictions of a half-space cooling model. While these recent studies raise the possibility of age-dependent proxies for the oceanic LAB (e.g., vertical gradient in shear-wave speed, azimuthal anisotropy, and radial anisotropy), the depths of these proxies are highly dependent on the choice of parameters, and it is uncertain whether global tomography models constructed from mostly land-based datasets have sufficient resolution in oceanic regions (e.g., Kawakatsu and Utada, 2017). To improve the resolution and advance our understanding of the oceanic LAS, we need to obtain the oceanic upper mantle structure incorporating surface wave data that traverse purely oceanic paths.

Portable broadband ocean bottom seismometers (BBOBSs) have been available for about two decades (e.g., Suetsugu and Shiohara, 2014), and many large-scale array observations with BBOBSs have been conducted in the Pacific Ocean (e.g., the Stagnant Slab project, the Hawaiian PLUME project). To date, more than 200 BBOBSs have been deployed in the Pacific Ocean. These seismometers provide data that allow us to improve the horizontal and vertical resolutions of the upper mantle structure beneath the Pacific Ocean. In the present study, we analyze the three-dimensional radially anisotropic shear-wave structure beneath the Pacific Ocean, using the method of Yoshizawa and Kennett (2004), which employs finite frequency tomography along with ray bending to create multi-mode phase-speed maps of Love and Rayleigh waves.

2. Data

We collected three-component broadband seismograms recorded in and around the Pacific Ocean from 1990 to 2014 by permanent land stations from the Ocean Hemisphere network Project (OHP), Incorporated Research Institutions for Seismology (IRIS), F-net broadband seismic network, South Pacific Broadband Seismic Network (SPANET), and LDG/CEA (Commissariat à l'Énergie Atomique), as well as ten temporary stations in French Polynesia, deployed by the PLUME project (Barruol, 2002), and four temporary stations deployed around the Ontong Java Plateau (Richardson et al., 2000).

We also collected broadband seismograms recorded by BBOBSs. The Japanese BBOBS group has conducted several temporary seafloor array deployments since 1999, using more than 100 BBOBS instruments; i.e., 17 in French Polynesia by the PLUME and TIARES projects (Suetsugu et al., 2009; Takeo et al., 2016); 34 in and around the Philippine Sea as part of the Stagnant Slab project (Shiobara et al., 2009); 33 in the northwestern Pacific Ocean for the NOMan project (Takeo et al., 2018); and 31 in the northwestern Pacific Ocean for other projects (Isse et al., 2006; Shito et al., 2013; Toneygawa et al., 2013).

Several major research projects in the United States have also deployed temporary BBOBS instruments; 10 land and 73 BBOBS

stations were placed in and around the Hawaiian islands during the Hawaiian PLUME project (Laske et al., 2009); 10 in the northwestern Pacific Ocean for PLATE project (Shintaku et al., 2014); and 21 in the central part of the Pacific Ocean during the NoMelt project (Lin et al., 2016).

We selected events with M_w or $m_b \geq 5.5$ and stations located in and around the Pacific Ocean (Fig. 1). Each record is first deconvolved with the corresponding instrumental response. We estimated directions of horizontal components of BBOBSs from the first arrival of P-waves that exhibit particle motion ellipticity of less than 0.1 for multiple events with $M_w \geq 6.5$.

3. Method of surface wave tomography

We employ surface-wave tomography, comprising three independent stages: (1) measurement of path-specific multimode phase-speed dispersion curves through nonlinear waveform fitting; (2) two-dimensional phase-speed mapping for each dispersion branch, incorporating finite-frequency and ray-bending effects; and (3) one-dimensional inversion of multimode phase dispersions at each grid point for a radially anisotropic, three-dimensional shear-wave speed model. Details are described by Yoshizawa and Kennett (2004) and Yoshizawa (2014). Here we briefly describe the method, focusing on details that differ from the original studies.

3.1. Measurement of the multimode phase-speed dispersions

In the first stage, we measured the path-specific phase speeds of Love and Rayleigh waves from the fundamental mode to the 4th higher mode, using a fully non-linear waveform inversion method (Yoshizawa and Ekström, 2010), in which the Neighbourhood Algorithm (NA) of Sambridge (1999) is used as a global optimizer that explores the model parameter space. Path-averaged one-dimensional reference models were constructed using PREM (Dziewonski and Anderson, 1981) with the crustal structure of 3SMAC (Nataf and Ricard, 1996). The waveform fitting process is fully automated, and the quality of the obtained dispersion curves is judged by a reliability parameter, determined by the degree of waveform fitting and the relative power of each mode in the chosen band-pass filtered time window. This empirical criterion is the same as that of Yoshizawa and Ekström (2010), except for the number of models using the NA (5050 in this study) and the start times of the time windows used to calculate the waveform misfit. A group speed of 7.2 km/s is adopted in the present study. To retain only high-quality dispersion curves, we apply the Grubbs test for outlier detection and removal, using three thresholds for path similarity: events and stations must be located within radii of 5° , 15° , and 30° , respectively.

The phase dispersion measurements as a function of frequency are plotted in Fig. 2 for each mode of Love and Rayleigh waves. We have analyzed about 300,000 waveforms for land stations and 60,000 waveforms for BBOBSs. We obtained, at most, $\sim 14,000$ paths for fundamental mode surface waves in the frequency range 5–30 mHz and 2000–9000 paths for higher modes. About 2% and 10% of Love and Rayleigh wave dispersion data were taken from BBOBS records, respectively. Fig. S1 shows ray distribution examples for the fundamental Love and Rayleigh waves at an 83-s period. In the present study, tilt and compliance noise corrections are not applied, which might increase the number of Rayleigh wave measurements in the future.

The oceanic upper mantle structure is slightly different from the PREM model. The arbitrary selection of the reference mantle model may possibly affect the measurements, especially with respect to Love waves (e.g., Nettles and Dziewonski, 2008). To assess such effects, we measured the path-averaged phase speeds using alternative reference models based on the PA5 model (Gaherty

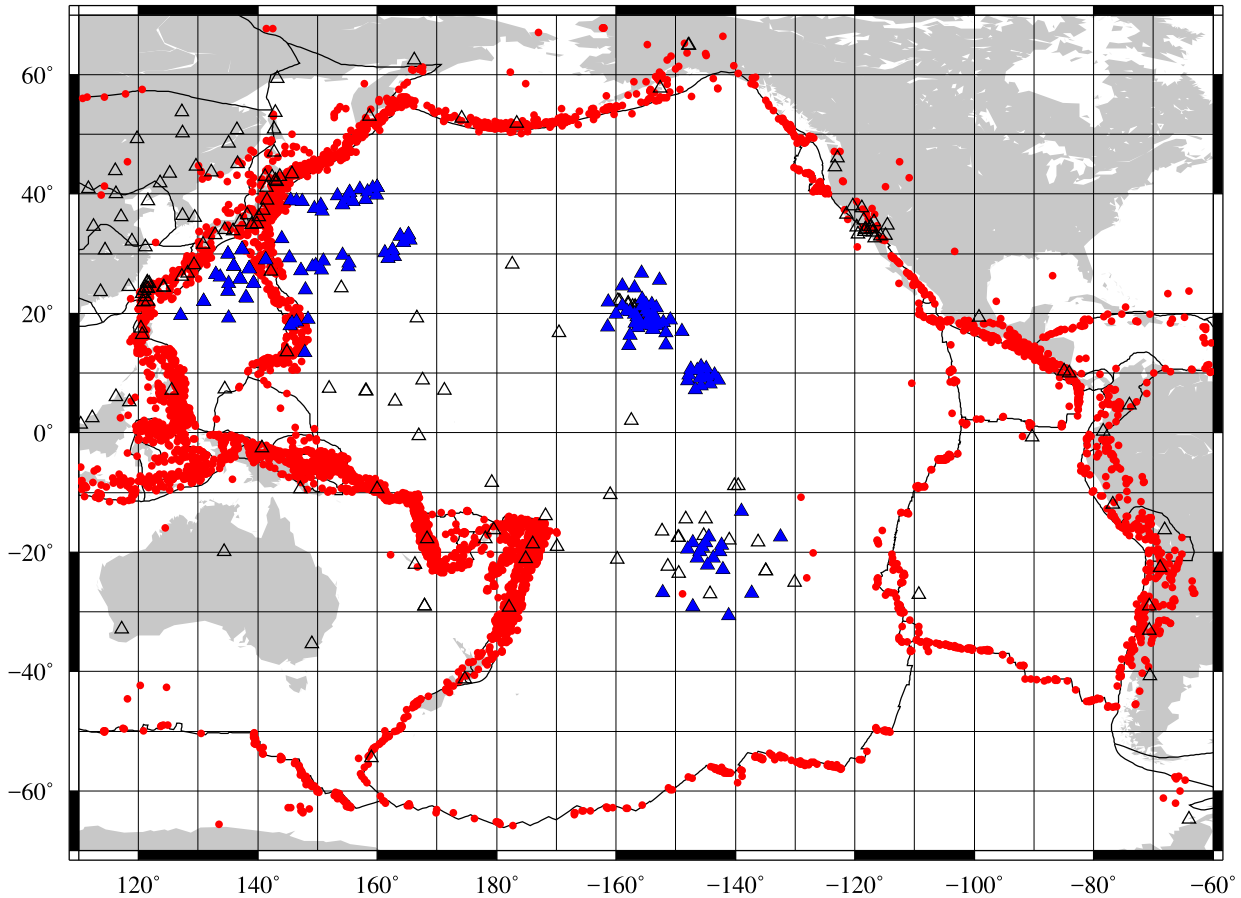


Fig. 1. Locations of the stations (triangles) and earthquakes (red circles) used in the present study. Blue and open triangles show the BBOBS and land stations, respectively. Black solid lines indicate the plate boundaries from Bird (2003). (For interpretation of the colors in the figure(s), the reader is referred to the web version of this article.)

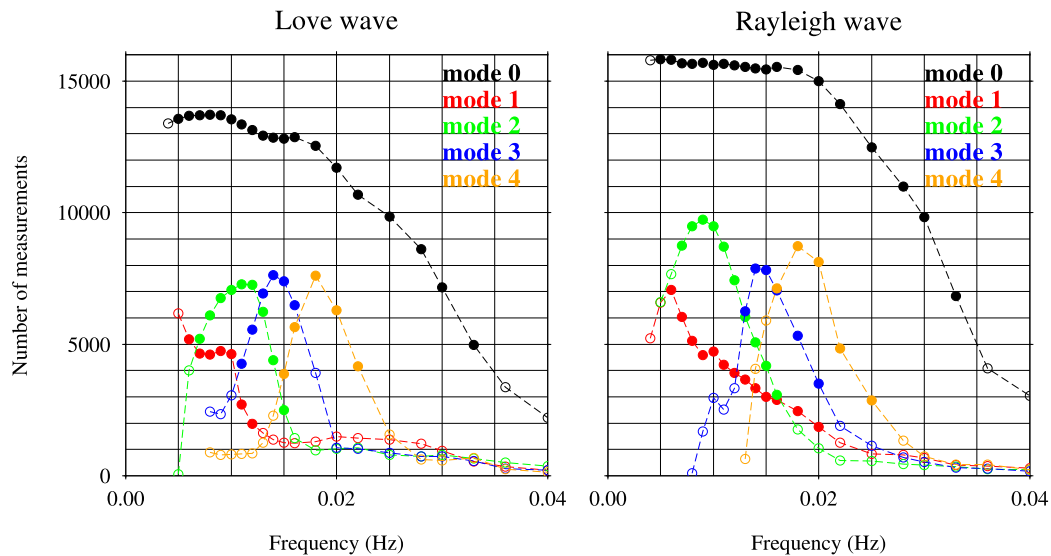


Fig. 2. Number of measurements for the Love and Rayleigh waves, up to the 4th higher mode, as a function of frequency, after applying quality control to the automated phase speed measurements (see the text for details). Solid circles show the data used in the subsequent phase speed mapping.

et al., 1999), which better represents the oceanic structure (i.e., lid and LVZ), along with the 3SMAC crust model, for waveforms recorded at KIP station in Hawaii. These waveforms contain rays that pass mainly through oceanic areas. Phase speeds of about 400 paths were successfully measured. The average of the differences in phase-speed measurements up to the 4th higher modes of the same events, using the PREM and PA5 models, are less than 0.2%,

and the standard deviation is less than 0.5% with no systematic difference. Since we use a fully nonlinear waveform fitting approach, the fast-lid structure can naturally be included in our parameter space. We further estimate the reliability of phase-speed measurements that represent how each mode can be separated from other overlapped modes. These may help in our robust measurements, irrespective of the employed reference model.

3.2. Phase-speed maps

In the second stage, we inverted path-specific multimode phase speeds for two-dimensional phase-speed maps at each frequency, incorporating the ray-path deviation from the great circle path and the finite-frequency effect (Yoshizawa and Kennett, 2004). Phase-speed maps are expanded in a set of B-spline functions with a rectangular grid whose interval in each map varies from 2–6°, depending on the number of paths and size of the Fresnel zone for each mode and frequency. As there are more seismic stations and events used in this study in the western Pacific, the ray paths are denser in the western Pacific and sparser in the eastern Pacific (Fig. S1). To further balance the uneven ray distribution and emphasize the effects of adding BBOBS data, whose deployment periods typically 1 yr, resulting in a small number of phase-speed measurements per station, we weighted Rayleigh wave data by a multiplicative factor of 2.0 and Love wave data by a factor of 3.0 from events with longitudes greater than 190°E, latitudes outside the range 50°N–40°S, or data recorded by a BBOBS (see section S1 of the Supplementary Material). Checkerboard resolution tests suggest that the lateral resolutions of the entire Pacific Ocean are $\sim 15^\circ$ for the isotropic structure and $\sim 18^\circ$ for the radially anisotropic structure in the present study, while that of the western Pacific Ocean are $\sim 8^\circ$ and $\sim 10^\circ$, respectively (see section S1 of the Supplementary Material). Therefore, we apply a spatial low-pass filter at 15° for isotropic structure and 18° for radially anisotropic structure to the results discussed for the entire Pacific region, and 8° and 10° , respectively, for the western Pacific.

To estimate standard errors of phase-speed maps, we performed a jackknife error estimation (see section S2 of the Supplementary Material). The estimated errors are less than 0.02 km/s for fundamental mode, and 0.05 km/s for higher modes in most regions, and are small enough for constructing shear wave speed models in the next stage.

Azimuthal anisotropy is not considered in this study. The anisotropic effect is assumed to average out when rays come from various directions, as in the case of this study of the Pacific Ocean.

3.3. Shear-wave speed model

In the third stage of our analysis, we inverted multimode phase-speed maps to generate a three-dimensional radially anisotropic shear-wave speed model, employing the iterative least-squares inversion of Tarantola and Valette (1982). Horizontal and vertical polarized S wave speeds, β_H and β_V at each location were obtained with corrections for the crustal structure, using the CRUST1.0 model (Laske et al., 2013). The details of the method are described by Yoshizawa (2014). To reconstruct a radially anisotropic speed structure, we use the linearized formulation for local phase speeds with six model parameters $[\rho, \alpha_H, \alpha_V, \beta_V, \beta_H, \eta]$: ρ is density; α_H and α_V are the horizontally and vertically polarized P wave speeds, respectively; β_H and β_V , are previously mentioned; and η is the conventional dimensionless anisotropic parameter. As for η , we do not incorporate the newly defined robust parameter (Kawakatsu, 2016). We use β_V and β_H as independent parameters, and the remaining four parameters are estimated by assuming a conventional scaling relationship for the shear-wave parameters, based on the work by Montagner and Anderson (1989): $\delta\rho/\rho = 0.3\delta\beta_{\text{iso}}/\beta_{\text{iso}}$, $\delta\alpha/\alpha = 0.5\delta\beta_{\text{iso}}/\beta_{\text{iso}}$, $\delta\phi/\phi = -1.5\delta\xi/\xi$, $\delta\eta/\eta = -2.5\delta\xi/\xi$, where β_{iso} is the Voigt-averaged isotropic shear wave speed, $\beta_{\text{iso}}^2 = (2/3)\beta_V^2 + (1/3)\beta_H^2$, and $\xi = (\beta_H/\beta_V)^2$. Yoshizawa (2014) pointed out that the results of inversions using β_V and ξ as independent parameters tend to be affected by the reference model, while those using β_V and β_H are less affected, due to the limited sensitivities of the Love wave phase speeds to the ξ parameter.

In this inversion, the degree of perturbation and the smoothness of the depth variations are controlled by two a priori parameters: the standard deviation σ and correlation length L , which are respectively set to 0.01 km/s and $L = 3$ km in the crust, 0.04 km/s and 15 km between the Moho and 400-km depth, and 0.03 km/s and 15 km between 400- and 670-km depth. The σ decreases linearly from 0.03 km/s at 670 km to 0.02 km/s at 1500 km, and L increases from 15 km at 670-km depth to 30 km at 1500-km depth. We confirmed L and σ through a series of synthetic tests, varying L and σ to see whether the retrieved models are consistent with various input models. Our one-dimensional reference speed model is modified from PREM by smoothing the 220-km discontinuity. We correct for the anelastic effect, using the attenuation model of PREM with a reference frequency of 1 Hz.

4. Model analysis: incorporation of the seafloor-age dependence

In the oceanic regions, the seafloor-age dependence of the seismic structure in the upper mantle has been widely accepted (e.g., Nishimura and Forsyth, 1989; Ritzwoller et al., 2004), incorporated in our tomography model. In this study, we first calculate the three-dimensional shear-wave speed structure with no assumption of age dependence, as described in section 3. Then, the age-dependent phase-speed maps are constructed from the structure. We then re-evaluate the two-dimensional phase-speed maps, using age-dependent initial models in the tomographic inversion to obtain a three-dimensional structure.

4.1. Estimating the age-dependent reference model

We first apply three-stage surface wave tomography with constant initial phase speed in the second stage of the inversion procedure, as in our previous studies (Isse et al., 2006, 2009). The resultant three-dimensional shear-wave model (PAC-c model) shows that the isotropic part exhibits a clear age dependence and generally follows isotherms predicted by a half-space cooling (HSC) model (Fig. S4). We next construct an age-dependent shear-wave model for the Pacific Plate region based on an HSC model: we apply a potential temperature of 1350 °C, a thermal diffusivity of 2.5×10^{-6} km²/yr, and an adiabatic gradient of 0.3 °C/km, using equations (15) and (17) in Faul and Jackson (2005). For given depths, the bin-averaged shear-wave speed as a function of the HSC model geotherm depends linearly on the seafloor age between 35 and 80 Ma, with slopes of -2.70×10^{-4} , -2.54×10^{-4} , and -2.43×10^{-4} km/s °C at depths of 50, 75, and 100 km, respectively (Fig. S5). We choose -2.54×10^{-4} km/s °C as the thermal coefficient, which describes the effects of temperature at a given depth. For other effects on the wave speed, we refer empirically to the shear-wave speed depth profile for the 50-Ma seafloor.

Next we construct age-dependent shear-wave speed reference profiles (Age-ref model) for the Pacific Ocean from the bin-averaged 50-Ma profile of the PAC-c model. For a given seafloor age, the HSC thermal model is used to estimate the differential temperature profile from the 50-Ma seafloor, and shear-wave speed corrections are applied using the thermal coefficient. The radially anisotropic profile is set to that of the 50-Ma seafloor, since the seafloor-age dependence of radial anisotropy is relatively small (e.g., see Fig. S4b). Using the Age-ref model and the seafloor age model of Müller et al. (2008), we calculate two-dimensional age-dependent phase-speed maps of Love and Rayleigh waves up to the 4th higher modes, for the Pacific Ocean. For regions where seafloor age is not available, an age of 50 Ma is assigned. Using these maps as initial models in estimating the phase-speed maps, we update the phase-speed maps and then obtain a renewed three-dimensional radially anisotropic shear-wave speed tomography model (PAC-age model). A comparison of the PAC-c and

PAC-age models indicates that the locations of anomalous regions are nearly the same in both models, but their amplitudes are not (Fig. S6). The differences are large in the shallower part, and the amplitude of the difference is mostly less than 1% shallower than at 75 km. In the PAC-age model, fast anomalies beneath Hawaii become weaker by approximately 1%, while other fast anomalies become stronger by at most 1%, compared to the PAC-c model. We could have applied further iterative updates to the shear-wave speed model by repeating the above procedure, but the difference between the PAC-age model and renewed models is less than 0.04%, indicating that one iteration is sufficient to improve the model.

5. Results

5.1. Shear-wave speed model

We first present the large-scale three-dimensional upper mantle structure of the entire Pacific Ocean after applying a spatial two-dimensional FFT low-pass Gaussian filter at 15° (*grdfft* in GMT; Wessel and Smith, 1991). The isotropic structure in Fig. 3 exhibits slow anomalies along ridges and in the back-arc basins, while fast anomalies exist in the western half of the Pacific Ocean at depths above 100 km. At depths below 150 km, slow anomalies are present beneath the Hawaii islands and the South Pacific Superswell, while fast anomalies are associated with the subducting Pacific Plate along the Kuril, Japan, and Izu–Bonin–Mariana trench system. At a depth of 150 km, fast anomalies can be seen in the northwestern Pacific Ocean. The radial anisotropy model in Fig. 3 shows that ξ at lithospheric depths is close to one; i.e., the lithosphere is nearly isotropic in the western half of the Pacific Ocean. Regions of $\xi > 1.0$ (i.e., $\beta_H > \beta_V$) are found along ridges and in the Philippine Sea plate, Nazca plate, and Cocos plate, and $\xi < 1.0$ is exhibited east of the Hawaiian Islands. At depths between 100–150 km, a large high- ξ area exists in the center of the Pacific, including the Hawaiian Islands and French Polynesia regions.

Compared with previous global tomography models (*savani* (Auer et al., 2014), SEMum2 (French et al., 2013), BYSX14 (Beghein et al., 2014), SAW642ANb (Panning et al., 2010), and ND2008 (Nettles and Dziewonski, 2008)), whose datasets and inversion methods are different from each other, large-scale anomalies, including slow anomalies along the ridge at shallow depths and fast anomalies in the western Pacific Ocean, at depths shallower than 150 km, are consistent with our model. However, regional-scale anomalies, including fastest anomalies in the Pacific plate at shallow depth and slow anomalies associated with hotspots at deeper depths, are different between models (Fig. S7). Our model is consistent with *savani* in many aspects. As for the anisotropic structure, previous models, except for SAW642ANb, have a peak amplitude at depths between 100 and 150 km, which is also seen in our model (Fig. S8). However, peak amplitudes, sizes, and locations of strong radial anisotropy are different among the models. There still is room for improvement in the study of radial anisotropic structure.

The depth profile across the Pacific Ocean (Fig. 4) shows the following features: (1) low-velocity zone beneath the East Pacific Rise is shallow; (2) fast-speed lid overlying the LVZ is clearly seen in Fig. 4a–d; (3) slow anomalies are evident at depths below 100 km beneath the Hawaiian Islands; (4) fast anomalies can be seen at depths shallower than 150 km around the Shatsky Rise (Fig. 4a); (5) radial anisotropy is relatively small in the fast-speed lid; (6) strong radial anisotropy ($\beta_H > \beta_V$) exists in the LVZ at depths of 100–200 km beneath the Hawaiian Islands and is shallower toward the EPR (Fig. 4a–b); and (7) depth of the peak of radial anisotropy beneath the Hawaiian Islands is slightly shallower than that of the LVZ (Fig. 4a–b).

The presence of azimuthal anisotropy may affect the result of tomography when the distribution of ray azimuths is not uniform. Ray paths in the eastern Pacific Ocean between the Hawaiian Islands and California are denser than in the surrounding regions (Fig. S1c). The azimuths of these rays are nearly parallel to the fast axis of the azimuthal anisotropy, whose peak-to-peak amplitude is about 2–3% (e.g., Debayle and Ricard, 2013). The obtained isotropic shear-wave speeds are 1.0–1.5% faster because of the unmodeled effects of azimuthal anisotropy. In the Pacific Superswell region, the azimuthal distribution of ray paths is relatively uniform, and thus, the negative residuals there are not artifact.

We now focus on the smaller-scale upper-mantle structure in the western Pacific Ocean, where the horizontal resolution is $\sim 8^\circ$ (Fig. 5). A remarkable contrast in isotropic speeds at depths shallower than 100 km can be seen between the old Pacific plate (80–170 Ma) and the young back-arc basins, i.e., the Philippine Sea Plate (0–65 Ma) and the Caroline Plate (0–30 Ma). In the Philippine Sea Plate, the old western part (30–65 Ma) is faster than the young eastern part (0–30 Ma), as suggested by Isse et al. (2009).

In the older areas of the Pacific Plate, the fastest anomalies at depths less than 75 km are not located in the oldest seafloor (170–180 Ma, ~ 1500 km east of Guam), but occur southeast of the Shatsky Rise, where the seafloor age is 130–150 Ma (Fig. 5). South of the oldest seafloor, in a region with ages of 150–160 Ma, a relatively slow region can be seen beneath, at depths shallower than 100 km. This suggests that the evolution of the Pacific lithosphere is slightly complex. At greater depths, we can identify fast anomalies along the Kuril, Japan, and Izu–Bonin–Mariana trenches, associated with the subducting Pacific Plate. The fast anomalies around the Shatsky Rise remain at depths of 200 km, and strong slow anomalies exist beneath the Hawaiian Islands.

In terms of radial anisotropy (Fig. 5), high ξ areas exist in the Philippine Sea and Caroline Plates at less than 100 km depths, and beneath the Hawaiian seamount and the Caroline islands at depths between 75 and 200 km. Relatively low ξ (~ 1) can be found in the Pacific Plate at 50- and 75-km depths. Isse et al. (2010) shows high ξ in the northwestern Pacific, which may be caused by using the fundamental mode only and the dependency of the initial model.

5.2. Depths of peak values of vertical shear-wave speed gradient

Recent studies have treated the depth of the negative peak in the vertical gradient of the shear-wave speed ($-d\beta/dz$)_{max} as a proxy measure of the depth of the LAB or transition (e.g., Burgos et al., 2014; Yoshizawa, 2014). We performed a series of synthetic tests in which a sharp decrease in shear-wave speed occurs from 40 to 160 km, by creating a lid with speeds 3% faster than the anisotropic smoothed PREM model (Fig. S9). Synthetic dispersion curves for Love and Rayleigh waves up to the 4th higher modes are calculated from these speed models, and the synthetic β_H and β_V models are inverted in a procedure similar to the inversion of the observed data, as outlined above. The synthetic models exhibit peak depths at 60–80 km for shallow-discontinuity inputs and 110–120 km for deep inputs. Such synthetic results can be affected by model parameterization and a priori smoothing constraint, so the vertical velocity gradient may not provide a stable or reliable estimate of a sharp discontinuity like oceanic LAB. We, therefore, use it only as one of the indices in the seismological depth profiles.

For the entire Pacific Ocean, the geographical distributions of the depths of negative peaks in the gradient suggest depths of ~ 40 km around the ridge areas and ~ 80 km in the older region of the northwestern Pacific (Fig. 6a). In the latter region, deeper negative peaks (~ 100 km) are located below the Ontong Java Plateau, the Mid-Pacific Mountains, and the Daito Ridges, anomalous re-

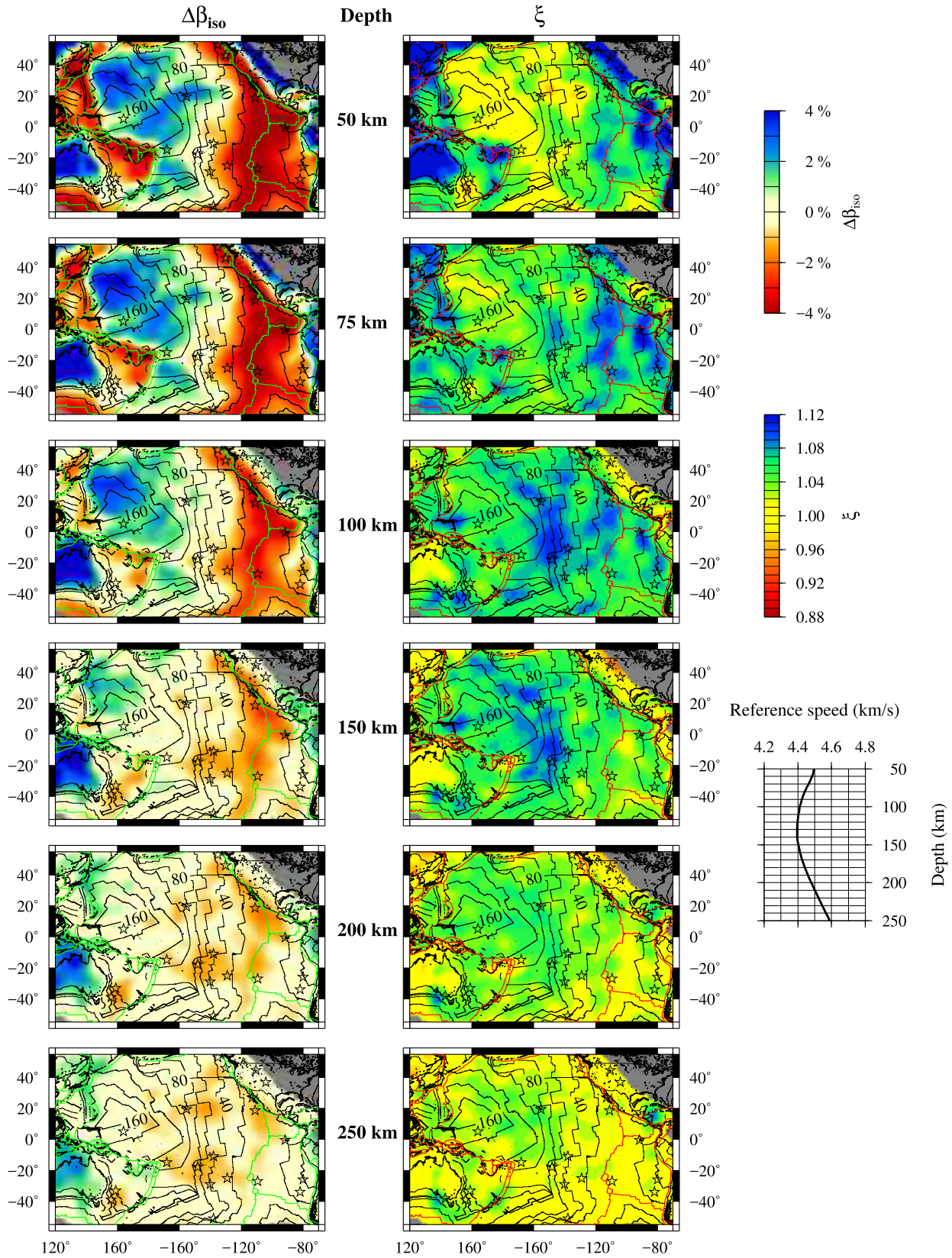


Fig. 3. Three-dimensional isotropic shear-wave speed (β_{180}) and radial anisotropy ($\xi = (\beta_{SH}/\beta_{SV})^2$) maps of the Pacific Ocean at depths between 50 and 250 km after spatial low-pass filtering at 15° and 18° , respectively. Thin solid lines show the seafloor ages at 40-Myr intervals. Open stars show the hotspots (Steinberger, 2000). Green lines in β_{180} and red lines in ξ indicate the plate boundaries.

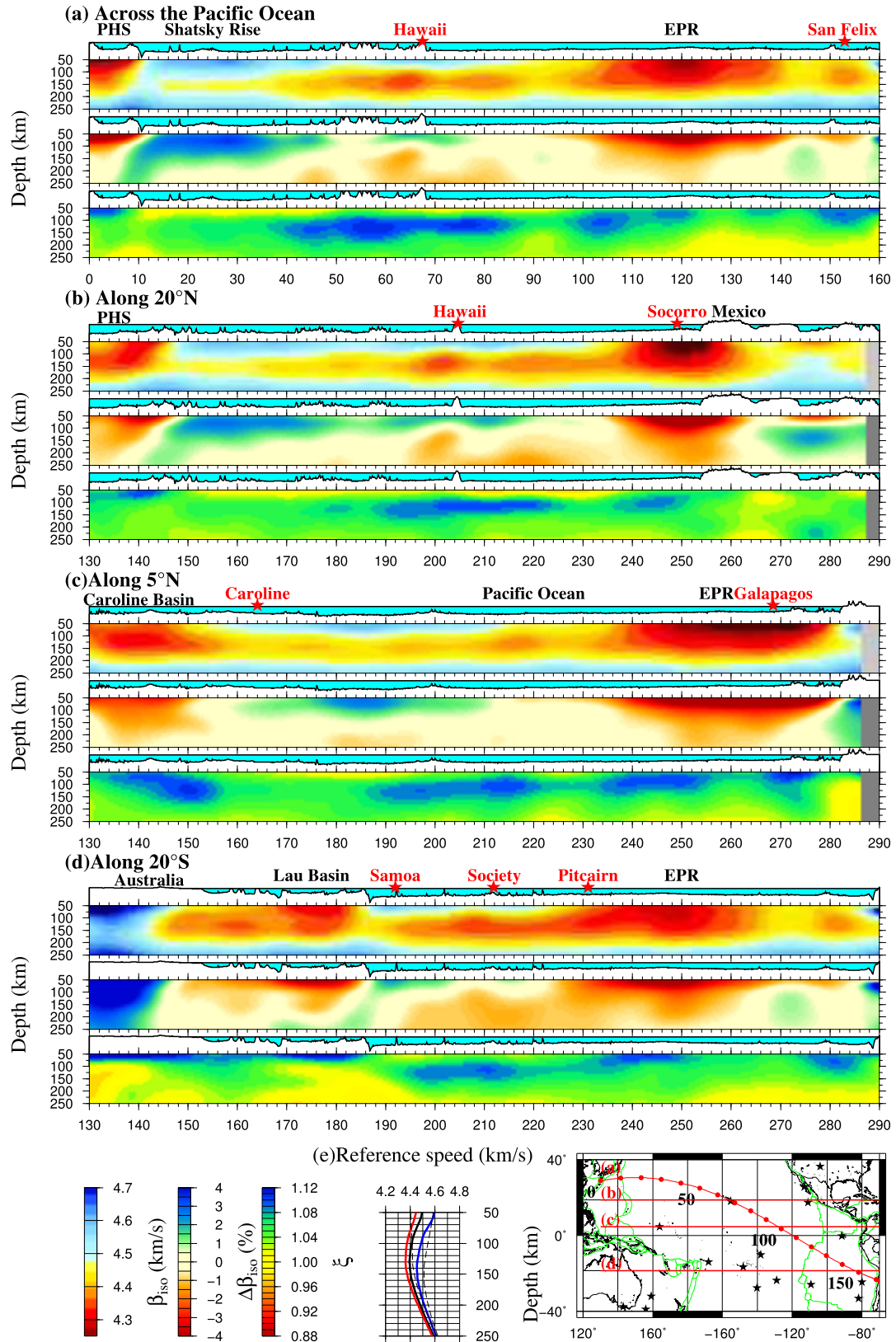


Fig. 4. Vertical profiles of shear-wave speed and radial anisotropy along (a) the great circle from Japan to South America across the Hawaiian Islands, (b) 20°N, (c) 5°N, and (d) 20°S. In each subfigure, the upper panel shows the isotropic shear-wave speed, the middle panel shows the perturbation of shear-wave speed from the reference model, and the lower panel shows the radial anisotropy. Annotated red stars and annotations indicate the hotspots near the cross lines. (e) Reference shear-wave speeds of β_{SH} (blue), β_{SV} (red), and β_{iso} (solid black lines). Broken lines indicate the β_{SH} and β_{SV} speeds in the initial model. The geographical map indicates the location of each vertical profile. The x axes indicate distances in degree from the beginning point in (a) and the longitudes in (b)–(d).

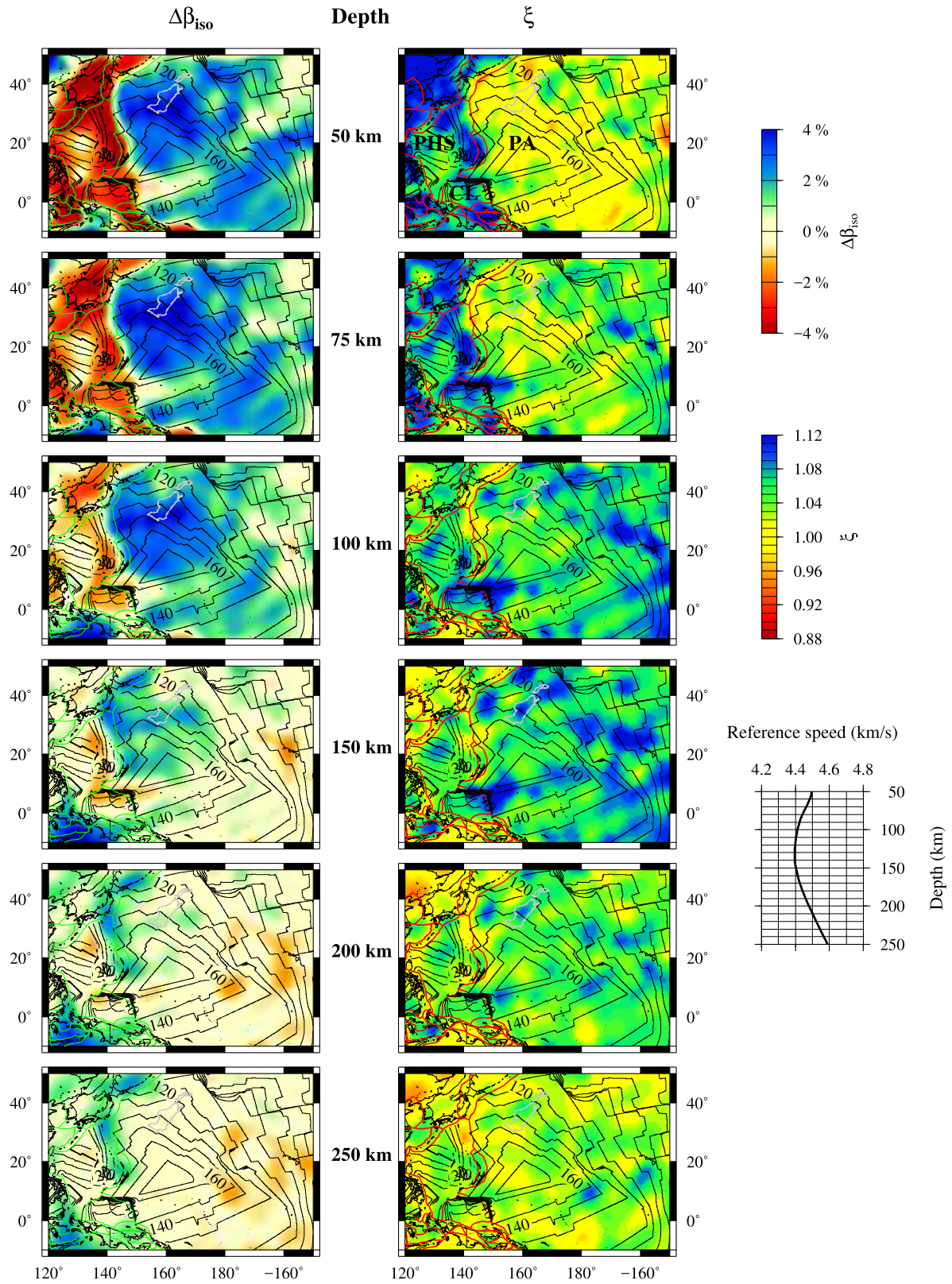


Fig. 5. Isotropic shear-wave speed and radial anisotropy maps in the western Pacific Ocean at depths between 50 and 250 km after applying a spatial low-pass filter at 8° and 10° , respectively. Gray lines show 5000 m seafloor contours of the Shatsky Rise. Thin solid lines show the seafloor ages in Ma. Green lines in β_{iso} and red lines in ξ indicate the plate boundaries. The Philippine Sea Plate (PHS), Caroline Plate (CL), and Pacific Plate (PA) are indicated in ξ at depths of 50 km.

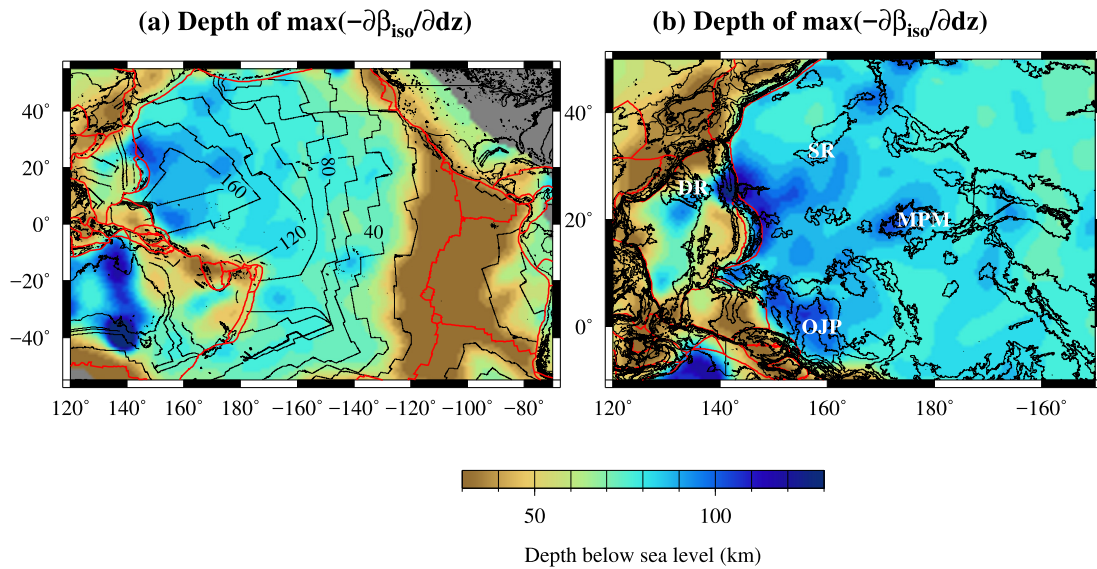


Fig. 6. Maps of the depths of the negative peaks of β_{iso} (a) in the entire Pacific Ocean after applying a spatial low-pass filter at 15° and (b) in the western Pacific Ocean after applying a spatial low-pass filter at 8° . DR: Daito Ridges; MPM: Mid-Pacific Mountains; OJP: Ontong Java Plateau; SR: Shatsky Rise. Thin black lines in (a) indicate the seafloor age, whereas lines in (b) indicate bathymetric contours from -5000 and -1000 m in 1000 m intervals. Red lines indicate the plate boundary.

regions with thick crusts (Fig. 6b). Deep negative peaks can also be seen along the Izu–Bonin–Mariana trench, where the Pacific Plate subducts beneath the Philippine Sea Plate. In the Philippine Sea Plate, the depth of the peak is ~ 50 km beneath the young seafloor (0–30 Ma) in the eastern half of the plate and ~ 80 km beneath the old seafloor (30–65 Ma) in the western half.

6. Discussion

6.1. Improvement in phase dispersion curves by adding BBOBS data

To determine the effect of including BBOBS data, we calculate the shear-wave speed structure, applying the same procedure for the PAC-age model by using phase-speed data without BBOBS measurements (PAC-age-exOBS). Large differences between PAC-age and PAC-age-exOBS models can be seen around the Shatsky rise, Hawaiian Islands, and eastward of those islands, where rays of BBOBS are concentrated (Figs. S1 and S10). Checkerboard tests indicate that the resolution in the northwestern Pacific Ocean improves when BBOBS data are added (Fig. 7), and the large difference mentioned above is located in an improved resolution area. For confirmation, we compare direct *in situ* phase dispersion measurements of the fundamental mode Rayleigh waves beneath two arrays of the NOMan project (Takeo et al., 2018), with regionally averaged phase-dispersion curves estimated by our tomographic procedure. As part of the NOMan project, two arrays were deployed, northwest and southeast of the Shatsky Rise (areas A and B in Fig. 8c). Significant improvement is evident, particularly for area B (Fig. 8a–b). In the case of the PAC-c model, the difference between measurements is large in area B (Fig. 8). The near-perfect consistency in area B is due, in part, to the introduction of the age-dependent reference model (section 4.1), thereby confirming the adequacy of our inversion approach as well as the inclusion of seafloor observation data.

6.2. Age-dependent profiles of shear-wave speed

Fig. 9 shows age-bin-averaged profiles of isotropic shear-wave speed and radial anisotropy in the Pacific Plate from the PAC-age model. The regions of fast shear-wave speed at shallow depths thicken progressively with age, and the shear-wave speed contour

of 4.45 km/s follows the 1100°C isotherm of the half-space cooling model (Fig. 9a). Our results are consistent with those of Maggi et al. (2006), who concluded that their profiles were broadly compatible with the HSC model. They also suggested that the apparent flattening of age-averaged profiles (e.g., Ritzwoller et al., 2004) might be an artifact due to insufficient path coverage in the central Pacific Ocean. Our age-averaged profiles of shear-wave speed have improved the path coverage because of the large number of BBOBS stations, which do not strongly depend on the choice of seafloor for averaging (e.g., avoid anomalous crust areas) or on the averaging scheme (mean or median). Our profiles are consistent with the inferences of Maggi et al. (2006). Standard deviation of the averaged shear-wave speed is less than 0.05 km/s ($<1\%$) for most seafloor ages; the exception are ages of 80–90 and 140–170 Ma, at depths shallower than 100 km (Fig. 9b). The fast anomalies around Hawaii and slow anomalies south of oldest seafloor are the causes of these large deviations, respectively.

Radially anisotropic structure seems to be less influenced by seafloor age. Fig. 9c shows that the radial anisotropy is weaker at shallower depths and stronger at greater depths (~ 120 km) in the LVZ. The weaker radial anisotropy region at depths shallower than 80 km may thicken with age, though the age dependence seems to be small compared to the shear-wave speed. The standard deviation of ξ is less than 0.03 for most regions; the exceptions are ages around 100 Ma at depths deeper than 150 km. The relatively weak radial anisotropy at shallow depths might not seem consistent with the observation of strong azimuthal anisotropy by active source analyses. The active source studies, however, analyze the structure just beneath the Moho, where there is no resolution in this study (note that our models are for below 40 km). Also, recent studies using *in situ* array measurements have revealed that the strength of the azimuthal anisotropy weakens with depth (Takeo et al., 2016, 2018; Lin et al., 2016).

The depths of negative peaks in the vertical speed gradient are also less age-dependent than the profiles of shear-wave speed. For seafloor ages less than 30 Ma, the depths of the peaks show a rapid increase, then increase slightly from 70 to 80 km, corresponding to seafloor ages between 40 and 170 Ma (Fig. 9a). Considering the non-linear biases in the depth estimates of the negative peaks seen in the synthetic tests (Fig. S9), we abstain from further discussion of this index parameter, but the estimated

6° checkerboard resolution test

(a) All data

(b) Land data only

(c) Difference

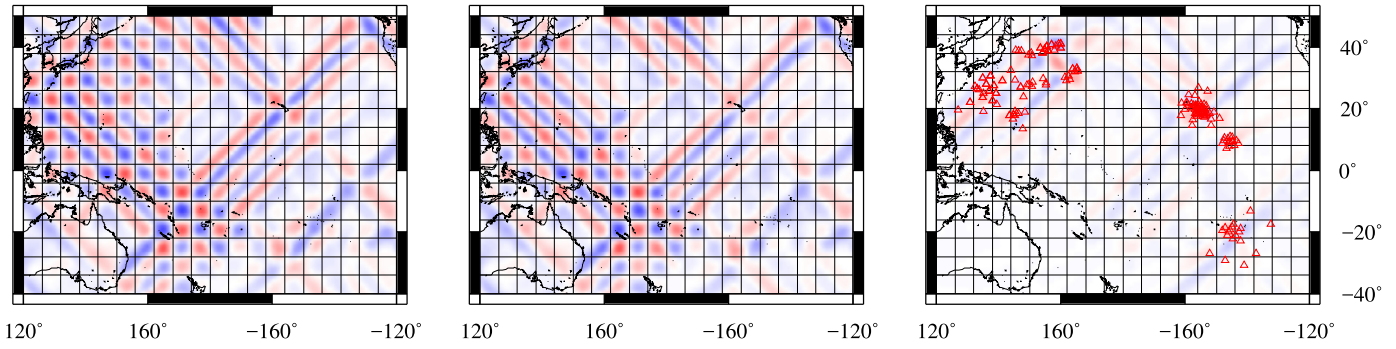


Fig. 7. Result of the checkerboard resolution tests for the fundamental mode of Rayleigh waves at a period of 83 s with 6° cells using (a) all data (as in Fig. S3e), (b) only land data, and (c) the difference between (a) and (b).

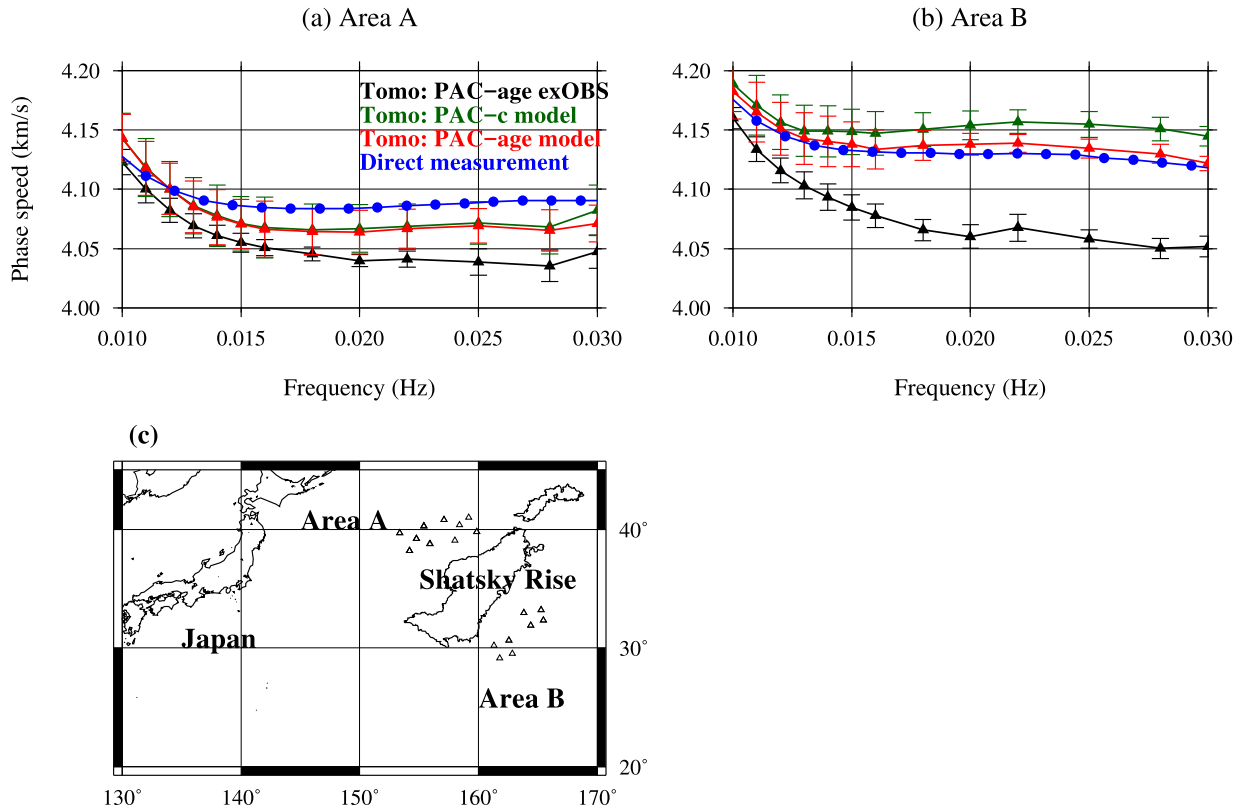


Fig. 8. Phase speed measurements of the fundamental mode of Rayleigh wave for (a) Area A and (b) Area B of the NOMan project. Direct measurements by Takeo et al. (2018) are shown by the blue symbols. Black symbols represent the phase speeds derived from our tomographic models without BBOBS data. Red symbols are from the PAC-age tomographic model. Green symbols are from the PAC-c model. Error bars indicate the one-standard deviations in each observation area. (c) Location map of the BBOBS arrays of the NOMan project.

depths are generally consistent with the local *in situ* array measurements estimated from BBOBS data. For example, the depth of the transition zone from the lid to the LVZ is 40–70 km beneath the 15–30 Ma Shikoku Basin (Takeo et al., 2013), 50–80 km beneath the 60–80 Ma seafloor of the Pacific Plate (Lin et al., 2016; Takeo et al., 2016), and 60–80 km beneath the 130–140 Ma seafloor (Takeo et al., 2018).

6.3. Reference Pacific speed model and anomalous oceanic upper-mantle regions

Based on the assumption that shear-wave speed in the upper mantle is controlled mainly by temperature and pressure, we now assess where the anomalous oceanic mantle is located in the

Pacific Ocean. Similar to section 4.1, we first estimate, via linear regression, the dependence of the shear-wave speed on temperature at a fixed depth, using the age-bin-averaged PAC-age model of the Pacific Plate region, with seafloor ages between 35 and 80 Ma, in which the presence of melt or some additional reheating effect is unlikely (Fig. 10a). The mantle temperature is calculated for the same HSC model as in section 4.1. The thermal coefficients are -3.66×10^{-4} , -3.55×10^{-4} , -3.61×10^{-4} , and -5.33×10^{-4} km/s.°C at depths of 50, 75, 100, and 150 km, respectively, which are nearly the same except at 150-km depth, where the linearity is worse than in the other profiles. The dG/dT (GPa/K) estimated from our model is -0.0111 , -0.0107 , -0.0107 , and -0.0158 . Laboratory data by Faul and Jackson (2005) used -0.0136 , which is not far from our estimation. Priestley and

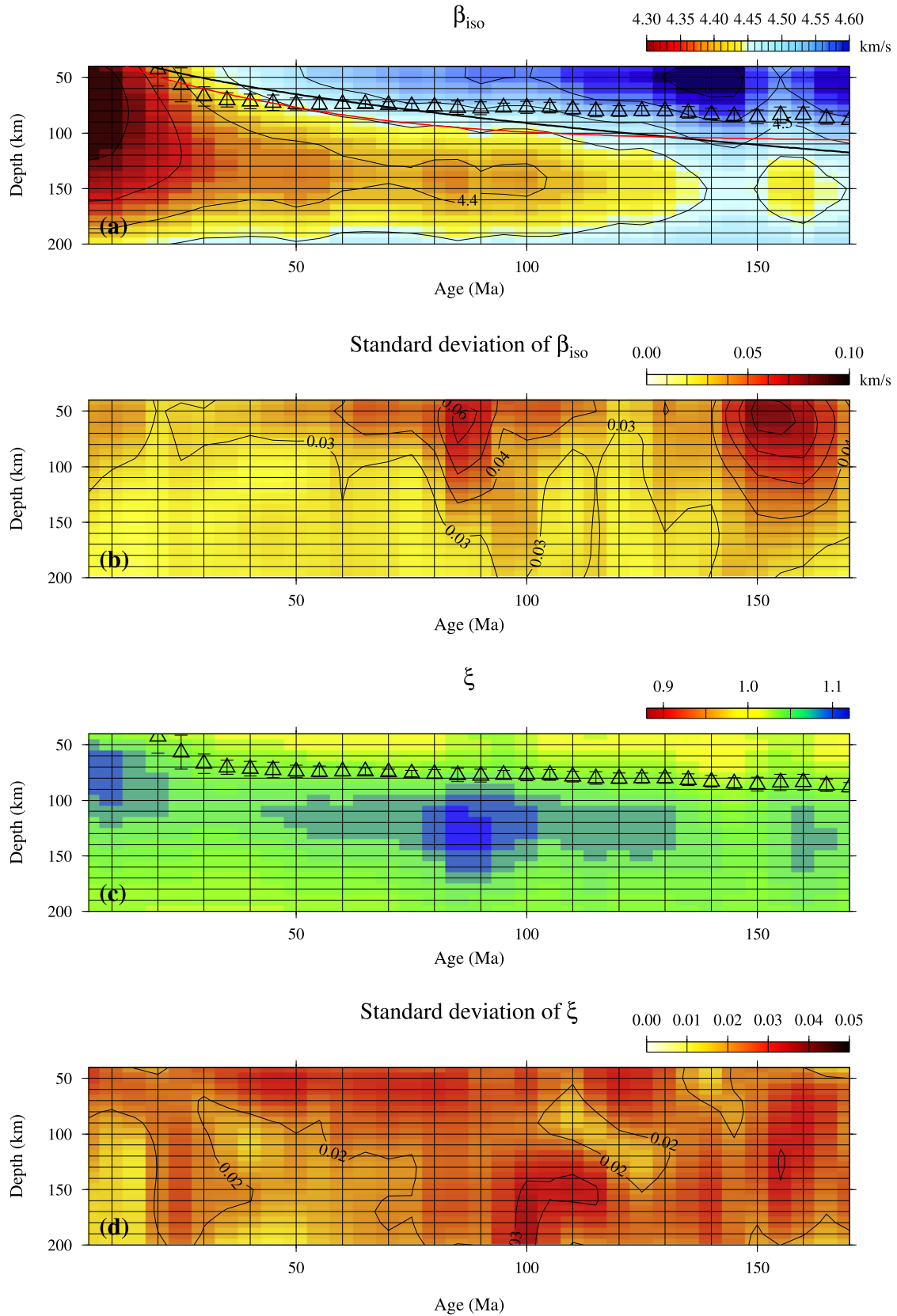


Fig. 9. (a) Age-bin-averaged isotropic shear-wave speed profiles, (b) corresponding one-standard deviation, and (c) age-bin-averaged radial anisotropy, (d) corresponding one-standard deviation profiles of the Pacific Plate. Open triangles show the average depth of the negative peaks of β_{iso} with a 10-Ma range, and error bars indicate one-standard deviation. In (a), the thin black contour lines show shear-wave speeds at 0.05 km/s intervals, and the thick black and red lines show the 1100°C and 1200°C isotherms taken from the HSC model used in our modeling, and from the plate model of Parsons and Sclater (1977), respectively.

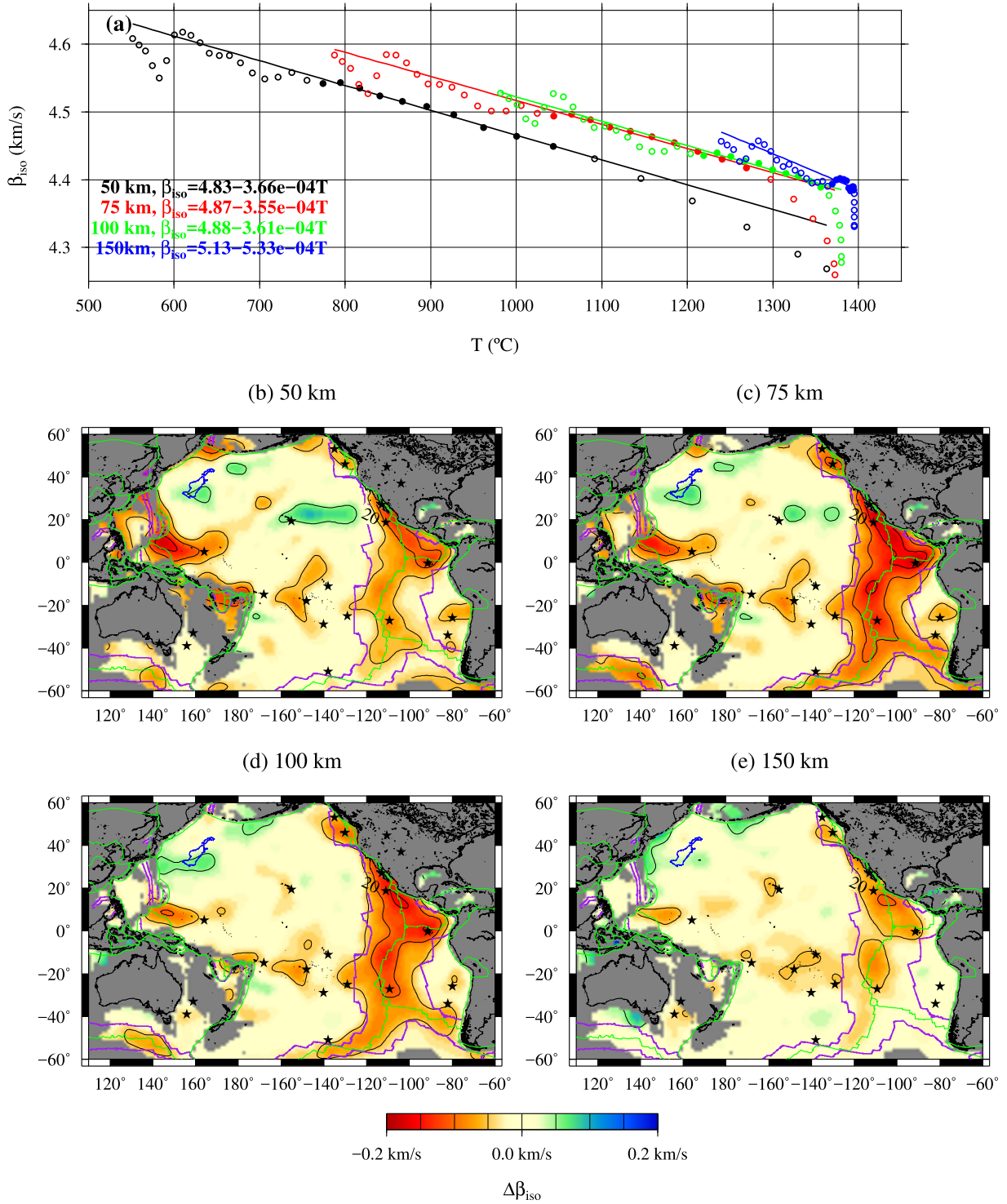


Fig. 10. (a) β_{iso} as a function of the geotherm based on the HSC model at 5-Myr intervals. Solid circles show the data at ages between 35 and 80 Ma, from which we estimated the thermal coefficient of β_{iso} . Solid lines show the predicted shear-wave speed profile calculated with the equations shown in the figure. Different colors indicate different depths. Geographical maps show the residuals after subtracting the predicted β_{iso} from the obtained values shown in Fig. 3 (with a spatial low-pass filter of 15°) at depths of (b) 50, (c) 75, (d) 100, and (e) 150 km. Purple lines indicate a seafloor age of 20 Ma, green lines show the plate boundaries, and solid stars indicate the hotspots. The contour interval is 0.05 km/s; the contours for 0.0 km/s are not plotted.

McKenzie (2013) estimated the unrelaxed shear modulus and its derivatives with respect to pressure and temperature, using shear-wave tomography models and a variety of geophysical and petrological observation and models. They obtained dG/dT of -0.00871 to -0.01668 depending on tomography models, consistent with our estimation. Data obtained far away from the regression lines

at high temperature (seafloor age younger than 35 Ma) are likely due to non-thermal effects.

The existence of melt, water content, and/or compositional differences may affect the results. If these exist uniformly, the constant terms can be affected. If there is a temperature dependence, thermal coefficients can be affected. The obtained regression lines

suggest a reference speed model based on the HSC model but not a purely thermal structure model.

Using the regression results shown in Fig. 10a, we construct reference shear-wave speed maps using the HSC thermal model and the seafloor age of the entire Pacific Ocean under the assumption of constant diffusive cooling during the evolution of the LAS. Deviations from a constant rate could indicate differences in physical properties (e.g., mantle composition, melting) and/or thermal properties (e.g., local cooling, reheating) (Fig. 10b–e). Compared with the shear-wave speed anomaly maps of Fig. 3, large-scale age-dependent anomalies associated with thermal structures are diminished in Fig. 10b–e, allowing easy identification of deviated regions. Residuals in most regions are less than 0.05 km/s ($\sim 1\%$) at all depths. This suggests that perturbations in the thermal structure based on the HSC model are smaller than 140 °C. The residuals are generally <0.05 km/s, not only in the Pacific Plate, for which we estimated the thermal coefficients, but also in the other surrounding oceanic plates. This might mean that the thermal evolution of the LAS beneath the Pacific Ocean is generally controlled by the same conditions in all areas; i.e., a similar mantle potential temperature. Ritzwoller et al. (2004) showed the temperature structure of the upper mantle beneath the entire Pacific using the phase-speed data of Love and Rayleigh waves based on the HSC model. They showed that the temperature structure was not consistent with the HSC temperature model for ages older than 70 Ma because of reheating that occurred between 70 and 100 Ma in the Central Pacific. In our result, the average shear-wave speeds are slower than the predicted profiles, which can be explained by the reheating. However, residual maps indicate that the residuals do not correlate with seafloor age, suggesting that these residuals are caused by local events.

There are some regions, on the other hand, where residuals are larger than 0.05 km/s. Dalton et al. (2014) suggest that the potential temperature variation along the ridge is 100–150 °C. The spatial resolution of our model is not enough to assess these ridge variations, so here, we consider regions with residuals larger than 0.05 km/s as anomalous regions. Large negative residuals can be seen along the ridges where seafloor ages are less than 20 Ma, in part of the Pacific Superswell region, around the Caroline hotspot, and near the San Felix and Juan Fernandez hotspots in the Nazca Plate (older than 20 Ma). In the ridge regions, residuals can be explained by partial melting or premelting (Yamauchi and Takei, 2016). In the Pacific Superswell region, these can be explained by high mantle temperatures caused by mantle plumes (e.g., Suetsugu et al., 2009). Using the obtained thermal coefficients, this region is estimated to be ~ 200 °C hotter than the reference model, consistent with the results of Suetsugu et al. (2009) who showed that the Society hotspot in the Pacific Superswell is 150–200 °C hotter than surroundings in the mantle transition zone. The negative residuals along the periphery of the western Pacific Ocean may be artifacts caused by smearing of slow shear-wave speeds in the surrounding regions. There are conspicuous negative residuals in the Caroline hotspots and its western Caroline Ridge, one of the submarine Large Igneous Provinces (LIPs). The hotspot track extends westward between 0 and 35 Ma, and the Caroline Ridge was constructed by the hotspot volcanism (Wu et al., 2016). The reference geotherm at the depth of 50 km in this area (150 Ma) is ~ 600 °C and the geotherm beneath the ridge is ~ 1050 °C, if the ridge was formed at 35 Ma. The 450 °C temperature difference indicates a ~ 0.1 km/s shear-wave speed difference. The obtained residuals are, thus, well explained by the evolution of the Caroline Ridge. There are no significant negative residuals along other hotspot tracks, which may be caused by the anomalies being smaller than the spatial resolution of our model and a small temperature difference between hotspot tracks and surroundings. Large positive residuals (>0.05 km/s) can be seen around the Hawaiian Islands, elongated

in the east–west direction in the zone between the Murray and Molokai fracture zones and the northwestern Pacific Ocean. The large residuals located around the Hawaiian Islands only exist at depths shallower than 75 km, whereas those in the northwestern Pacific remain at a depth of 150 km. The large positive residuals in the northwestern Pacific Ocean are located southeast of the Shatsky Rise, which is another LIP. No similar high positive residuals are found beneath other LIPs, which may suggest that the cause of the residuals is not associated with the generation process of the LIPs. The positive anomalies around the Hawaiian Islands are possibly caused by artificial effects as discussed above. There are many possibilities to explain the positive residuals, such as lower temperature, lower amount of water, and/or compositional difference, compared with the reference model.

A plate model whose thermal plate thickness of ~ 150 km is another possible thermal model (Fig. 9a). When we estimated the mantle temperature using the plate model of Parsons and Sclater (1977) (PSM model), for which the plate thickness is 125 km, large residuals of deviation maps are also located in the same area as those by the HSC model (Fig. S11). At shallower depths, the thermal structures of the HSC and PSM models are similar, so their residuals are similar. At a depth of 150 km, positive residuals in the northwestern Pacific Ocean are enlarged, but the area of the strongest positive anomalies is the same. This indicates that the thermal model is not as sensitive to detecting anomalous oceanic upper mantle regions.

7. Conclusions

We analyze the three-dimensional radially anisotropic shear-wave speed structure in the upper mantle beneath the Pacific Ocean, using a surface-wave tomography technique in which multimode phase speeds of surface waves are measured and inverted by incorporating finite-frequency and ray-bending effects. We used BBOBS data and data from broadband seismic stations on land in and around the Pacific Ocean to obtain a radially anisotropic shear-wave model of the upper mantle beneath the Pacific Ocean. We also update the model, incorporating the effects of the seafloor-age dependence. The obtained model shows that the fastest anomalies at depths shallower than 100 km are not located beneath the oldest seafloor but instead lie southeast of the Shatsky Rise. Strong radial anisotropy can be seen in the central Pacific at depths of 100–200 km. Synthetic experiments indicate that the negative gradient of shear-wave speed may not provide a stable and reliable estimate of the depth of the rapid transition from the lithosphere to the asthenosphere in oceanic areas. Isotropic shear-wave speed structure shows age dependence and is well-approximated by a half-space cooling model. From age-bin-averaged shear-wave speed profiles and the HSC model, we estimate the thermo-speed relationship in the Pacific Plate to construct maps in the Pacific Ocean of deviation from a reference age-dependent shear-wave speed model. The result indicates that most of regions show small residuals (<0.05 km/s). Large negative residuals, which might be explained by partial melt, anelasticity, and/or hot mantle plumes, are located along the ridge and beneath hotspots, and large positive residuals are found south of the Shatsky Rise. The incorporation of the age-dependent reference model and OBS data greatly improves the accuracy of local phase-speed estimates of tomography, evidenced by a direct comparison with *in situ* array measurements.

Acknowledgements

We wish to thank the staff of OHRC, IRIS, OBSIP, Geoscope, SPANET, Geoscience Australia, GEOFON, and the LDG/CEA data centers for their efforts in maintaining and managing the seismic stations for which data were used in the present study. We also

thank the captains, officers, crews, and ROV operation team of the *R/V Kaiei* of JAMSTEC and the *W/V KAIYU* of Offshore Operation Co. Ltd., for enabling the success of the cruises. We also thank Dr. M. Panning and two anonymous reviewers for constructive reviews that improved the manuscript. The Japanese BBOBS data are available from the Ocean Hemisphere Project Data Management Center (<http://ohpdm.ceri.u-tokyo.ac.jp/>) of the Earthquake Research Institute, the University of Tokyo, and from Pacific21 (<http://p21.jamstec.go.jp/top/>) of the Japan Agency for Marine-earth Science and Technology. U.S. BBOBS Data were provided by instruments from the Ocean Bottom Seismograph Instrument Pool (<http://www.obsip.org>) which is funded by the National Science Foundation. OBSIP data are archived at the IRIS Data Management Center (<http://www.iris.edu>). This work was supported by a Grants-in-Aid for Scientific Research (KAKENHI, 19253004, 22000003, 16K05533, 30114698, 16253002, 26400443, and 18H03735) from the Japan Society for the Promotion of Science. The GMT software package (Wessel and Smith, 1991) was used in this study.

Appendix A. Supplementary material

Supplementary material related to this article can be found online at <https://doi.org/10.1016/j.epsl.2018.12.033>.

References

- Auer, L., Boschi, L., Becker, T.W., Nissen-Meyer, T., Giardini, D., 2014. Savani: a variable resolution whole-mantle model of anisotropic shear velocity variations based on multiple data sets. *J. Geophys. Res.* 119. <https://doi.org/10.1002/2013JB010773>.
- Barruol, G., 2002. PLUME investigates South Pacific Superswell. *Eos* 83, 511–514. <https://doi.org/10.1029/2002EO000354>.
- Beghein, C., Yuan, K., Schmerr, N., Xing, Z., 2014. Changes in seismic anisotropy shed light on the nature of the Gutenberg discontinuity. *Science* 343, 1237–1240. <https://doi.org/10.1126/science.1246724>.
- Bird, P., 2003. An updated digital model of plate boundaries. *Geochem. Geophys. Geosyst.* 4, 1027. <https://doi.org/10.1029/2001GC000252>.
- Burgos, G., Montagner, J.-P., Beucler, E., Capdeville, Y., Mocquet, A., Drilleau, M., 2014. Oceanic lithosphere–asthenosphere boundary from surface wave dispersion data. *J. Geophys. Res.* 119, 1079–1093. <https://doi.org/10.1002/2013JB010528>.
- Dalton, C.A., Langmuir, C.H., Gale, A., 2014. Geophysical and geochemical evidence for deep temperature variations beneath mid-ocean ridges. *Science* 344, 80–83. <https://doi.org/10.1126/science.1249466>.
- Debayle, E., Ricard, Y., 2013. Seismic observations of large-scale deformation at the bottom of fast-moving plates. *Earth Planet. Sci. Lett.* 376, 165–177. <https://doi.org/10.1016/j.epsl.2013.06.025>.
- Dziewoński, A.M., Anderson, D.L., 1981. Preliminary reference Earth model. *Phys. Earth Planet. Inter.* 25, 297–356.
- Faul, U., Jackson, I., 2005. The seismological signature of temperature and grain size variations in the upper mantle. *Earth Planet. Sci. Lett.* 234, 119–134. <https://doi.org/10.1016/j.epsl.2005.02.008>.
- French, S.W., Lekić, V., Romanowicz, B., 2013. Waveform tomography reveals channeled flow at the base of the oceanic asthenosphere. *Science* 342, 227–230. <https://doi.org/10.1126/science.1241514>.
- Gaherty, J.B., Kato, M., Jordan, T.H., 1999. Seismological structure of the upper mantle: a regional comparison of seismic layering. *Phys. Earth Planet. Inter.* 110, 21–41. [https://doi.org/10.1016/S0031-9201\(98\)00132-0](https://doi.org/10.1016/S0031-9201(98)00132-0).
- Isse, T., Shiobara, H., Montagner, J., Sugioka, H., Ito, A., Shito, A., Kanazawa, T., Yoshizawa, K., 2010. Anisotropic structures of the upper mantle beneath the northern Philippine Sea region from Rayleigh and Love wave tomography. *Phys. Earth Planet. Inter.* 183, 33–43. <https://doi.org/10.1016/j.pepi.2010.04.006>.
- Isse, T., Shiobara, H., Tamura, Y., Suetsugu, D., Yoshizawa, K., Sugioka, H., Ito, A., Kanazawa, T., Shinohara, M., Mochizuki, K., 2009. Seismic structure of the upper mantle beneath the Philippine Sea from seafloor and land observation: implications for mantle convection and magma genesis in the Izu–Bonin–Mariana subduction zone. *Earth Planet. Sci. Lett.* 278, 107–119. <https://doi.org/10.1016/j.epsl.2008.11.032>.
- Isse, T., Yoshizawa, K., Shiobara, H., Shinohara, M., Nakahigashi, K., Mochizuki, K., Sugioka, H., Suetsugu, D., Oki, S., Kanazawa, T., Suyehiro, K., Fukao, Y., 2006. Three-dimensional shear wave structure beneath the Philippine Sea from land and ocean bottom broadband seismograms. *J. Geophys. Res.* 111. <https://doi.org/10.1029/2005JB003750>.
- Kawakatsu, H., 2016. A new fifth parameter for transverse isotropy II: partial derivatives. *Geophys. J. Int.* 206, 360–367. <https://doi.org/10.1093/gji/ggw152>.
- Kawakatsu, H., Utada, H., 2017. Seismic and electrical signatures of the lithosphere–asthenosphere system of the normal oceanic mantle. *Annu. Rev. Earth Planet. Sci.* 45, 139–167. <https://doi.org/10.1146/annurev-earth-063016-020319>.
- Laske, G., Collins, J.A., Wolfe, C.J., Solomon, S.C., Detrick, R.S., Orcutt, J.A., Bercovici, D., Hauri, E.H., 2009. Probing the Hawaiian hot spot with new broadband ocean bottom instruments. *Eos* 90, 362–363. <https://doi.org/10.1029/2009EO410002>.
- Laske, G., Masters, G., Ma, Z., Pasyanos, M., 2013. Update on CRUST1.0 – a 1-degree global model of Earth's crust. *Geophys. Res. Abstr.* 15. Abstract EGU2013-2658.
- Lin, P.-Y.P., Gaherty, J.B., Jin, G., Collins, J.A., Lizarralde, D., Evans, R.L., Hirth, G., 2016. High-resolution seismic constraints on flow dynamics in the oceanic asthenosphere. *Nature* 535, 538–541. <https://doi.org/10.1038/nature18012>.
- Maggi, A., Debayle, E., Priestley, K., Barruol, G., 2006. Multimode surface waveform tomography of the Pacific Ocean: a closer look at the lithospheric cooling signature. *Geophys. J. Int.* 166, 1384–1397. <https://doi.org/10.1111/j.1365-246X.2006.03037.x>.
- Montagner, J.P., Anderson, D.L., 1989. Constrained reference mantle model. *Phys. Earth Planet. Inter.* 58, 205–227.
- Montagner, J.P., Tanimoto, T., 1991. Global upper mantle tomography of seismic velocities and anisotropies. *J. Geophys. Res., Solid Earth* 96, 20337–20351. <https://doi.org/10.1029/91JB01890>.
- Müller, R.D., Sdrölias, M., Gaina, C., Roest, W.R., 2008. Age, spreading rates, and spreading asymmetry of the world's ocean crust. *Geochem. Geophys. Geosyst.* 9. <https://doi.org/10.1029/2007GC001743>.
- Nataf, H.-C., Ricard, Y., 1996. 3SMAC: an a priori tomographic model of the upper mantle based on geophysical modeling. *Phys. Earth Planet. Inter.* 95, 101–122. [https://doi.org/10.1016/0031-9201\(95\)03105-7](https://doi.org/10.1016/0031-9201(95)03105-7).
- Nettles, M., Dziewoński, A.M., 2008. Radially anisotropic shear velocity structure of the upper mantle globally and beneath North America. *J. Geophys. Res.* 113. <https://doi.org/10.1029/2006JB004819>.
- Nishimura, C.E., Forsyth, D.W., 1989. The anisotropic structure of the upper mantle in the Pacific. *Geophys. J. Int.* 96, 203–229. <https://doi.org/10.1111/j.1365-246X.1989.tb04446.x>.
- Panning, M., Lekić, V., Romanowicz, B., 2010. Importance of crustal corrections in the development of a new global model of radial anisotropy. *J. Geophys. Res.* 115, B12325. <https://doi.org/10.1029/2010JB007520>.
- Parsons, B., Sclater, J.G., 1977. An analysis of the variation of ocean floor bathymetry and heat flow with age. *J. Geophys. Res.* <https://doi.org/10.1029/JB082i005p00803>.
- Richardson, W.P., Okal, E.A., Van der Lee, S., 2000. Rayleigh-wave tomography of the Ontong–Java Plateau. *Phys. Earth Planet. Inter.* 118, 29–51. [https://doi.org/10.1016/S0031-9201\(99\)00122-3](https://doi.org/10.1016/S0031-9201(99)00122-3).
- Priestley, K., McKenzie, D.P., 2013. The relationship between shear wave velocity, temperature, attenuation and viscosity in the shallow part of the mantle. *Earth Planet. Sci. Lett.* 381, 78–91. <https://doi.org/10.1016/j.epsl.2013.08.022>.
- Ritzwoller, M.H., Shapiro, N.M., Zhong, S.-J., 2004. Cooling history of the Pacific lithosphere. *Earth Planet. Sci. Lett.* 226, 69–84. <https://doi.org/10.1016/j.epsl.2004.07.032>.
- Sambridge, M., 1999. Geophysical inversion with a neighbourhood algorithm-I. Searching a parameter space. *Geophys. J. Int.* 138, 479–494. <https://doi.org/10.1046/j.1365-246X.1999.00876.x>.
- Schaeffer, A.J., Lebedev, S., Becker, T.W., 2016. Azimuthal seismic anisotropy in the Earth's upper mantle and the thickness of tectonic plates. *Geophys. J. Int.* 207, 901–933. <https://doi.org/10.1093/gji/ggw309>.
- Shintaku, N., Forsyth, D.W., Hajewski, C.J., Weeraratne, D.S., 2014. Pn anisotropy in Mesozoic western Pacific lithosphere. *J. Geophys. Res.* 119, 3050–3063.
- Shiobara, H., Baba, K., Utada, H., Fukao, Y., 2009. Ocean bottom array probes stagnant slab beneath the Philippine Sea. *Eos* 90, 70–71. <https://doi.org/10.1029/2009EO090002>.
- Shito, A., Suetsugu, D., Furumura, T., Sugioka, H., Ito, A., 2013. Small-scale heterogeneities in the oceanic lithosphere inferred from guided waves. *Geophys. Res. Lett.* 40, 1708–1712. <https://doi.org/10.1002/grl.50330>.
- Steinberger, B., 2000. Plumes in a convecting mantle: models and observations for individual hotspots. *J. Geophys. Res.* 105, 11127–11152. <https://doi.org/10.1029/1999JB900398>.
- Suetsugu, D., Isse, T., Tanaka, S., Obayashi, M., Shiobara, H., Sugioka, H., Kanazawa, T., Fukao, Y., Barruol, G., Raymond, D., 2009. South Pacific mantle plumes imaged by seismic observation on islands and seafloor. *Geochem. Geophys. Geosyst.* 10. <https://doi.org/10.1029/2009GC002533>.
- Suetsugu, D., Shiobara, H., 2014. Broadband ocean-bottom seismology. *Annu. Rev. Earth Planet. Sci.* 42, 27–43. <https://doi.org/10.1146/annurev-earth-060313-054818>.
- Takeo, A., Kawakatsu, H., Isse, T., Nishida, K., Shiobara, H., Sugioka, H., Ito, A., Utada, H., 2018. In-situ characterization of the lithosphere–asthenosphere system beneath NW Pacific Ocean via broadband dispersion survey with two OBS arrays. *Geochem. Geophys. Geosyst.* <https://doi.org/10.1029/2018GC007588>.
- Takeo, A., Kawakatsu, H., Isse, T., Nishida, K., Sugioka, H., Ito, A., Shiobara, H., Suetsugu, D., 2016. Seismic azimuthal anisotropy in the oceanic lithosphere and asthenosphere from broadband surface wave analysis of OBS array records at 60 Ma seafloor. *J. Geophys. Res.* 121, 1927–1947. <https://doi.org/10.1002/2015JB012429>.

- Takeo, A., Nishida, K., Isse, T., Kawakatsu, H., Shiobara, H., Sugioka, H., Kanazawa, T., 2013. Radially anisotropic structure beneath the Shikoku Basin from broadband surface wave analysis of ocean bottom seismometer records. *J. Geophys. Res.* 118, 2878–2892. <https://doi.org/10.1002/jgrb.50219>.
- Tarantola, A., Valette, B., 1982. Generalized nonlinear inverse problems solved using the least squares criterion. *Rev. Geophys.* 20, 219–232. <https://doi.org/10.1029/RG020i002p00219>.
- Tonegawa, T., Fukao, Y., Nishida, K., Sugioka, H., Ito, A., 2013. A temporal change of shear wave anisotropy within the marine sedimentary layer associated with the 2011 Tohoku-Oki earthquake. *J. Geophys. Res.* 118, 607–615. <https://doi.org/10.1002/jgrb.50074>.
- Wessel, P., Smith, W.H.F., 1991. Free software helps map and display data. *Eos* 72, 441–446. <https://doi.org/10.1029/90EO00319>.
- Wu, J., Suppe, J., Lu, R., Kanda, R., 2016. Philippine Sea and East Asian plate tectonics since 52 Ma constrained by new subducted slab reconstruction methods. *J. Geophys. Res.* 121, 4670–4741. <https://doi.org/10.1002/2016JB012923>.
- Yamauchi, H., Takei, Y., 2016. Polycrystal anelasticity at near-solidus temperatures. *J. Geophys. Res.* 121, 7790–7820. <https://doi.org/10.1002/2016JB013316>.
- Yoshizawa, K., 2014. Radially anisotropic 3-D shear wave structure of the Australian lithosphere and asthenosphere from multi-mode surface waves. *Phys. Earth Planet. Inter.* 235, 33–48. <https://doi.org/10.1016/j.pepi.2014.07.008>.
- Yoshizawa, K., Ekström, G., 2010. Automated multimode phase speed measurements for high-resolution regional-scale tomography: application to North America. *Geophys. J. Int.* 183, 1538–1558. <https://doi.org/10.1111/j.1365-246X.2010.04814.x>.
- Yoshizawa, K., Kennett, B.L.N., 2004. Multimode surface wave tomography for the Australian region using a three-stage approach incorporating finite frequency effects. *J. Geophys. Res.* 109. <https://doi.org/10.1029/2002JB002254>.